Ordering state in orthopyroxene as determined by precession electron diffraction

Damien Jacob,[1,]* Lukas Palatinus,[2] Priscille Cuvillier,[1] Hugues Leroux,[1]
Chiara Domeneghetti,[3] and Fernando Cámara[4]

[1]Unité Matériaux et Transformations, Université Lille1, CNRS UMR 8207, 59655 Villeneuve d'Ascq, France
[2]Institute of Physics of the Academy of Sciences of the Czech Republic, 182 21 Prague, Czech Republic
[3]Dipartimento di Scienze della Terra e dell'Ambiente, Università di Pavia, 27100-Pavia, Italy
[4]Dipartimento di Scienze della Terra, Università di Torino, 10125-Torino, Italy

Abstract

Fe^{2+} and Mg distribution on octahedral M1 and M2 sites of the orthopyroxene structure is an indicator of the cooling rate and closure temperature of the mineral. It is generally obtained by single-crystal X-ray diffraction, which is limited in spatial resolution. In this work, we determine the cationic distribution at a submicrometer scale in a transmission electron microscope using precession electron diffraction. Two orthopyroxene samples coming from the same metamorphic rock are studied, a naturally ordered one and a disordered one. The latter was obtained from the ordered sample by annealing at high temperature and rapid quenching. Both samples have been first studied in X-ray diffraction and then in precession electron diffraction. Intensities recorded in zone-axis precession electron diffraction experiments have been quantitatively analyzed and compared to simulations, taking into account dynamical interactions between diffracted beams. Our structure refinement results are in good agreement with those obtained by single-crystal X-ray diffraction. They enable to distinguish between the ordered sample and the disordered one in terms of the observed molar fractions of Fe at M1 and M2 sites. We discuss the sensitivity of the method as a function of experimental parameters. The larger dispersion of the results obtained on the ordered specimen is attributed to structural heterogeneities inherent to the sample.

Keywords: Ordering, orthopyroxene, precession electron diffraction, site occupancy, structure refinement, transmission electron microscopy

Introduction

Fe^{2+} and Mg distribution on octahedral M1 and M2 sites of the orthopyroxene (Opx) structure is an indicator of the cooling rate and closure temperature of the mineral (Ganguly 1982; Ganguly and Tazzoli 1994; Stimpfl et al. 1999, 2005). These data are of great importance, as they permit the retrieval of the thermal history of the crystal. The cationic distribution is generally accessible thanks to the quantitative analysis of diffracted intensities as obtained by X-ray diffraction (XRD), leading to the determination of atomic positions and site occupancies with a good accuracy. Nevertheless, XRD is limited in spatial resolution. Contradictory results in cooling rate determination based on site occupancies as determined by XRD have been explained by the occurrence of microstructural features such as local variations of composition, exsolution lamellae and Guinier-Preston zones (Zema et al. 1999; Cámara et al. 2000; Heinemann et al. 2008). These features can only be revealed by transmission electron microscopy, whereas XRD analysis generally leads to averaged information, which may induce misinterpretation.

In this work, we present results on site occupancy determination obtained at a microscopic scale in a transmission electron microscope (TEM) using precession electron diffraction (PED). Since its development in 1994 (Vincent and Midgley 1994),

PED has become an efficient and widely used method for solving structures of inorganic compounds [Boulahya et al. (2007), perovskite related $LaBaCuCoO_{5.2}$ and $Ba_6Mn_5O_{16}$; Gemmi and Nicolopoulos (2007), minerals uvarovite and åkermanite; Boullay et al. (2009), mineral brownmillerite; Mugnaioli et al. (2009), inorganic salt $BaSO_4$; Gemmi et al. (2010), titanate $Li_4Ti_8Ni_3O_{21}$; Hadermann et al. (2010), perovskite related $Pb_{13}Mn_9O_{25}$; White et al. (2010), tin oxide Sn_3O_4; Hadermann et al. (2011), mixed phosphate Li_2CoPO_4F; Klein (2011), oxides Mn_2O_3 and $PbMnO_{2.75}$; Palatinus et al. (2011), copper silicide-germanide $Cu_3(Si,Ge)$; Song et al. (2012), hydroxyapatite]. At this stage, solving a structure means determining its unit-cell parameters, its space group and the position of most of the atoms within the unit cell. Nevertheless, another important goal in structural analysis is the structure refinement, i.e., the accurate determination of all the atomic positions and their occupancy. Unlike X-rays, electrons interact strongly with matter and continuous exchange of electrons between transmitted and diffracted beams occurs when they are passing through the crystal, leading to so-called dynamical effects. Accurate simulation of electron diffraction data thus requires the use of dynamical diffraction theory. In this context, the main advantage of PED for structure solving is the reduction of the dynamical effects (Gjønnes et al. 1998; Eggeman et al. 2010; Sinkler and Marks 2010), making the intensities more related to the square of the structure factors of reflections. Nevertheless, to

---

* E-mail: Damien.Jacob@univ-lille1.fr

date very few attempts have been made to treat PED data using dynamical theory for structural refinement (Own et al. 2006; Oleynikov et al. 2007; Dudka et al. 2007; Sinkler et al. 2010). In most other cases the refinement was based on the comparison of experimental diffracted intensities with simulated ones calculated in the kinematical approximation, i.e., considering diffracted intensities as proportional to the square of the structure factors. The refinement results using kinematical approximation show that dynamical effects must be taken into account, if accurate structure parameters are needed. However, to our knowledge, only one structure refinement using dynamical theory has been reported (Dudka et al. 2007) with silicon as a test sample. In this work, we show that when the structure is partially known, dynamical analysis of intensities as obtained using PED leads to reliable and reasonably accurate determination of structural parameters such as atomic occupancy factors on specific sites of the structure. Applied to natural Opx samples, also characterized by single-crystal XRD, our PED analysis enables an unambiguous discrimination between an ordered sample (natural, untreated) and a disordered one (heat-treated and quenched).

EXPERIMENTAL METHODS

Specimen selection and heat treatments

The studied specimens are natural Opx $(Mg_{1.4}Fe_{0.6})Si_2O_6$ single crystals from granulite rocks of the Wilson Terrane, North Victoria Land, Antarctica [crystal label B22, Tribaudino and Talarico (1992)]. The ratio Mg/(Fe+Mg) is close to 0.70 as previously determined by electron microprobe (Tarantino et al. 2002). Small amounts of Ca and other minor elements such as Ti, Al, and Cr are also present. They were not considered in the present analysis. Four crystals were selected and used for the X-ray single-crystal diffraction to check for the homogeneity of the samples. To enable a direct comparison with disordered, but otherwise similar sample, two of these crystals have also been heated for 48 h at 1000 °C. They were sealed (after alternately washing with nitrogen flux and vacuuming) into a small silica tube together with an iron-wüstite buffer and then heated in a vertical furnace. Inside the silica tube, the crystals and the buffer were put into two small separate Pt crucibles to avoid contact between them. Heated samples were then quenched by dropping the tube into cold water. One untreated and one heat-treated crystals were then selected for TEM analysis.

X-ray single-crystal diffraction and structure refinement

Intensity data were collected at the Dipartimento di Scienze della Terra e dell'Ambiente, Università di Pavia, on a three-circle Bruker AXS SMART APEX diffractometer, equipped with a CCD detector (graphite-monochromatized MoKα radiation, λ = 0.71073 Å, 55 kV, 30 mA) and a monocap collimator. The Bruker SMART software package was used. A total of 3600 frames (frame resolution 512 × 512 pixels) were collected with four different goniometer settings using the ω-scan mode (scan width: 0.2° ω; exposure time: 5 s/frame; detector-sample distance: 4.02 cm). About 14 500 reflections were collected. Completeness of the measured data was achieved up to 37° θ. The Bruker SAINT+ software was used for data reduction, including intensity integration, background and Lorentz-polarization corrections. The semi-empirical absorption correction of Blessing (1995), based on the determination of transmission factors for equivalent reflections, was applied using the program SADABS (Sheldrick 1996). The unit-cell parameters were obtained by a least-squares procedure from the positions of about 8000 reflections in the θ-range 3–37°. The observed F_o^2 values were then treated with a full-matrix least-squares refinement in *Pbca* space group by SHELX-97 (Sheldrick 2008), using individual weights and the weighting scheme suggested by the program. No threshold or cutting of low-intensity reflections was applied, following the recommendations of Merli et al. (2002) suggested by the leverage analysis applied to the orthopyroxene. The atomic scattering curves were taken from *International Tables for X-ray Crystallography* (Ibers and Hamilton 1974). Neutral vs. ionized scattering factors were refined in all sites that are not involved in chemical substitutions (Hawthorne et al. 1995) and complete ionization for Mg and Fe in M1 and M2 sites was assumed. The extinction correction was applied using the procedures within the program SHELX-97. To get a better comparability of the

refinement results obtained using XRD and PED data, structure refinements from XRD data have also been achieved in the same conditions as previously described but limiting the resolution to that of PED data (*d* = 0.7124 Å).

TEM observations and precession electron diffraction

Thin foils for TEM observations were prepared from both the untreated and heat-treated samples. Slabs about 50 nm thick normal to the [001] orientation have been cut from the single-crystal grains by focused ion beam (FIB) technique (FEI Strata DB 235 FIB-FESEM) at IEMN (Institute of Micro and Nano Electronics, University Lille 1).

TEM observations were performed at University Lille 1 with a LaB$_6$ FEI Tecnai G2-20 operated at 200 kV and equipped with a DIGISTAR precession system (Nanomegas). In the PED technique, the incident beam is scanned at a constant precession semi-angle (ranging typically from 1 to 4°) around the optical axis, in combination with an opposite and synchronized descan of the transmitted and diffracted beams below the specimen (Vincent and Midgley 1994). During the precession movement, the reciprocal lattice nodes are thus swept through the Ewald sphere and integrated intensities over a large range of deviation parameter *S* around the Bragg orientation are collected (compare Fig. 7). In PED, the incident beam is never directed along the zone-axis so that dynamical interactions are reduced. Microdiffraction (MD) and selected-area electron diffraction (SAED) patterns have been acquired with the optical axis aligned parallel to the [001] zone axis of the crystal. MD patterns have been obtained using a nearly parallel probe of about 10–40 nm produced by a 10 μm condensor aperture. SAED patterns have been obtained using a defocused parallel beam and a circular aperture selecting an illuminated area of about 250 nm in diameter. Precession angles of 1.6° (heat-treated sample only), 2.4°, and 2.8° have been used to test the sensitivity of the method to the precession angle.

ANALYSIS OF PED DATA

Dynamical calculations of intensities

In a first approach, dynamical diffracted intensities have been calculated in the Bloch-wave formalism using the JEMS software by P. Stadelmann (2004). Then, for systematic comparison of simulated data with experimental ones and a search for the best agreement, an auxiliary program also using the Bloch-wave approach has been used. The full description of the program and simulation conditions are presented in a dedicated paper (Palatinus et al. 2013). Basically, the simulation of diffracted intensities is obtained as an incoherent summation of intensities sequentially calculated for a number N_{or} of orientations of the incident beam along the precession circuit. N_{or} is an important parameter of the simulation: the larger N_{or}, the more accurate is the result. A few tests have been performed probing the sensitivity of the simulated intensities on the choice of N_{or}. These tests showed that fixing N_{or} to 150 is appropriate, as no improvement of the match could be obtained with larger N_{or}. For a given structure file (see next paragraph), other main simulation parameters are the sample thickness *t*, the orientation of the precession hollow cone axis with respect to the crystal lattice and the number of diffracted beams to be taken into account for convergence. In this preliminary work, no refinement of the beam orientation with respect to the crystal orientation has been performed. We thus assumed that the crystal zone-axis used for the diffraction pattern collection was perfectly parallel to the precession cone axis (normally aligned along the optical axis of the microscope). This is generally not exactly fulfilled experimentally, but we will see in the results section that this approximation leads to reasonably accurate results provided the precession angle is sufficiently large. The number of beams included in the calculation is described by two parameters, the maximum length of the diffraction vectors g^{max} (in Å^{-1}) and the maximum excitation error

S_g^{max}. Following our preliminary tests and results from Palatinus et al. (2013), the values of g^{max} and S_g^{max} have been fixed to 2.0 and 0.02 Å^{-1}, respectively, leading to a good compromise between computation time and accuracy.

Comparison of simulated and experimental data

For comparison with simulated data, integrated intensities were extracted from experimental zone-axis patterns using the program PETS (Palatinus 2011; Palatinus et al. 2013). The output of the program consists of the list of reflections with their indices, intensities and estimated standard deviations of the intensities $\sigma(I)$ calculated using the standard background-signal-background method. Intensities were extracted up to $g^{max} = 1.4$ Å^{-1}. Typical values of the number of observed reflections ($I > 3\sigma$) are about 400, for about 500 total reflections. All the PED hkl files used in the present work are available as supplementary material[1]. The experimental data sets were then compared with several sets of simulated intensities calculated from the Opx structure with variable Fe molar fraction $X_{Fe}(M1)$ and $X_{Fe}(M2)$ on the M1 and M2 sites. Mg content is given by $X_{Mg}(M1) = 1 - X_{Fe}(M1)$ and $X_{Mg}(M2) = 1 - X_{Fe}(M2)$ as required by the pyroxene stoichiom-

etry $(Mg_{2-x}Fe_x)Si_2O_6$, with x = $X_{Fe}(M1) + X_{Fe}(M2)$ the total Fe content (considering that minor elements are not taken into account for this study; they account for <0.04 apfu, i.e., <2%). All other structural parameters are kept equal to the values deduced from XRD analysis (Table 1). No variation of the cell parameters as a function of the order parameter has been considered since this effect is negligible (Tarantino et al. 2002).

The present method is not a refinement method based on a least-square procedure but rather a grid search method. The best match between experimental and simulated intensities is assessed by the lowest value of the weighted residual value $wR2$ given by:

$$wR2 = \sqrt{\frac{\sum w_g (I_g^o - I_g^c)^2}{\sum w_g (I_g^o)^2}}$$

where I_g^o and I_g^c are the observed and calculated intensities, $w_g = \sigma^{-2} (I_g^o)$ and the summations run over all reflections from the experimental data set.

RESULTS

XRD structure refinements

Table 1 reports the structure refinement results obtained with the high-resolution data of both the untreated and heat-treated crystals. In Table 2 are summarized the atomic fractions of Mg and Fe^{2+} at the M1 and M2 sites and the degree of order expressed as $Q = X_{Fe}(M2) - X_{Fe}(M1)$ of the untreated and heat-treated

TABLE 1A. Structure refinement results obtained with the XRD high-resolution data from both the untreated and heat-treated crystals: Untreated crystal (high-resolution data)

a (Å)	b (Å)	c (Å)	Unit-cell volume (Å³)		Space group	
18.2810(7)	8.8732(4)	5.2070(2)	844.63(6)		Pbca	
			Structure parameters			
Site	x/a	y/b	z/c	Occupancy	U (Å²)	Site multiplicity
SiA	0.271544(14)	0.34092(3)	0.05148(5)	1	0.00664(6)	8c
SiB	0.473884(14)	0.33679(3)	0.79705(5)	1	0.00664(6)	8c
O1A	0.18346(4)	0.33838(8)	0.04147(14)	1	0.00799(12)	8c
O1B	0.56251(4)	0.33764(8)	0.79832(14)	1	0.00814(12)	8c
O2A	0.31114(4)	0.50118(8)	0.05038(15)	1	0.00948(12)	8c
O2B	0.43369(4)	0.48497(8)	0.69471(14)	1	0.00976(12)	8c
O3A	0.30269(4)	0.22822(9)	−0.17338(14)	1	0.01049(13)	8c
O3B	0.44727(4)	0.19933(9)	0.59741(15)	1	0.01011(12)	8c
M1(Fe²⁺)	0.375580(18)	0.65446(4)	0.87128(7)	0.029(2)	0.00754(11)	8c
M1(Mg²⁺)	0.375580(18)	0.65446(4)	0.87128(7)	0.971(2)	0.00754(11)	8c
M2(Fe²⁺)	0.378034(11)	0.48345(2)	0.36509(4)	0.554(2)	0.00981(7)	8c
M2(Mg²⁺)	0.378034(11)	0.48345(2)	0.36509(4)	0.446(2)	0.00981(7)	8c

TABLE 1B. Structure refinement results obtained with the XRD high-resolution data from both the untreated and heat-treated crystals: Heat-treated crystal (high-resolution data)

a (Å)	b (Å)	c (Å)	Unit-cell volume (Å³)		Space group	
18.3022(14)	8.8816(7)	5.2082(4)	846.6(1)		Pbca	
			Structure parameters			
Site	x/a	y/b	z/c	Occupancy	U (Å²)	Site multiplicity
SiA	0.271647(15)	0.34083(3)	0.05069(5)	1	0.00705(7)	8c
SiB	0.473781(15)	0.33678(3)	0.79655(6)	1	0.00699(7)	8c
O1A	0.18360(4)	0.33901(8)	0.03946(15)	1	0.00863(13)	8c
O1B	0.56236(4)	0.33842(8)	0.79762(14)	1	0.00870(13)	8c
O2A	0.31119(4)	0.50097(8)	0.04912(15)	1	0.01006(13)	8c
O2B	0.43343(4)	0.48423(8)	0.69310(15)	1	0.01035(13)	8c
O3A	0.30274(4)	0.22748(9)	−0.17301(14)	1	0.01083(13)	8c
O3B	0.44741(4)	0.19873(9)	0.59763(14)	1	0.01065(13)	8c
M1(Fe²⁺)	0.375724(15)	0.65432(3)	0.87012(6)	0.155(2)	0.00805(10)	8c
M1(Mg²⁺)	0.375724(15)	0.65432(3)	0.87012(6)	0.845(2)	0.00805(10)	8c
M2(Fe²⁺)	0.377827(12)	0.48401(3)	0.36401(4)	0.438(2)	0.01025(8)	8c
M2(Mg²⁺)	0.377827(12)	0.48401(3)	0.36401(4)	0.562(2)	0.01025(8)	8c

TABLE 2. Refined molar fractions of Fe and Mg on M1 and M2 sites of the orthopyroxene structure as deduced from XRD

	Untreated crystal		Heat-treated crystal	
	Full data set	Low res. 0.714 Å	Full data set	Low res. 0.714 Å
$X_{Fe}(M1)$	0.029(2)	0.028(3)	0.155(2)	0.154(3)
$X_{Mg}(M1)$	0.971(2)	0.972(3)	0.845(2)	0.846(3)
$X_{Fe}(M2)$	0.554(2)	0.555(3)	0.438(2)	0.439(3)
$X_{Mg}(M2)$	0.446(2)	0.445(3)	0.562(2)	0.561(3)
Mg/(Fe+Mg)	0.709(3)	0.709(3)	0.704(3)	0.704(3)
$Q = X_{Fe}(M2) - X_{Fe}(M1)$	0.525(3)	0.527(3)	0.283(3)	0.285(3)
R_1 (%)	2.73	2.41	3.07	2.66
wR2	6.64	5.99	7.41	6.81
no. of $I/\sigma > 4$	2090	1187	2039	1172
no. relf. tot.	2209	1209	2219	1215
ref. param.	93	93	93	93
GooF	1.199	1.172	1.144	1.178

crystals, together with the refinement parameters results. Results obtained limiting the resolution to that of PED data ($g^{max} = 1.4$ Å^{-1}) overlap within their error bars with those obtained with the full set of XRD data. The four crystallographic data of both crystals have been deposited[1]

The untreated crystals are characterized by a high degree of Fe^{2+}-Mg order on the octahedral sites M1 and M2 of the Opx structure, with M2 sites mainly occupied by larger Fe^{2+} cations. This ordered state is characteristic for slow cooling rate and low-closure temperature of the diffusion process (around 200 °C) associated with the metamorphic origin of the parent rocks (Tribaudino and Talarico 1992).

For the heat-treated samples, structure refinement results confirmed that the structure was disordered, with a higher degree of mixing of the Fe^{2+} on both M1 and M2 sites.

TEM samples description

At the TEM scale, the untreated sample exhibits a homogenous microstructure made of Opx containing a few planar defects and dislocations (Fig. 1a). The heat-treated sample shows evidence of incongruent melting located at the very surface of the sample, leading to a mixture of melt SiO$_2$ and Fe-rich olivine. The TEM study was performed in the lower part of the sample, for which Opx is found to be homogeneous (Fig. 1b).

Determination of cation occupancies by PED

PED [001] zone-axis patterns have been acquired on both samples at several defect-free areas separated by about 0.5 μm. Results are first presented for the heat-treated sample and then for the untreated one.
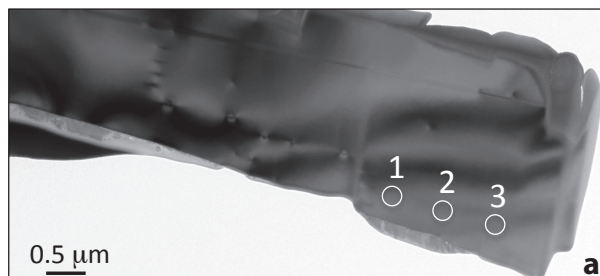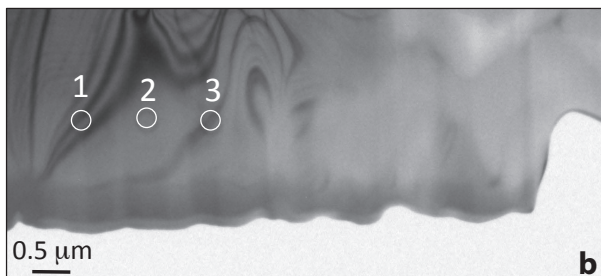
Heat-treated sample

Selected area PED patterns have been acquired at three areas of the sample (located by circles on Fig. 1b) and for precession angles of 1.6°, 2.4°, and 2.8° (Fig. 2). As described in the experimental section, the best match between experimental and simulated intensities is searched by varying three parameters: the sample thickness t and the occupancies $X_{Fe}(M1)$ and $X_{Fe}(M2)$. Results giving the best agreement (lowest wR2 values) are summarized in Table 3 and plotted in Figure 3. Uncertainty of the thickness is taken as a half of the thickness step between individual simulations (4 nm). In the present work, uncertainties of the occupancies are estimated as the variations of X_{Fe} leading to 0.1% variation on the minimum wR2 value. This estimation may appear as somewhat artificial, but it is directly related to the curvature of the wR2 surface as a function of $X_{Fe}(M1)$ and $X_{Fe}(M2)$ (Figs. 4a and 4b) and so to the actual sensitivity of the method as a function of the experimental parameters (mainly the precession angle). A more rigorous treatment based on a statistical analysis of the data as described in Palatinus et al.
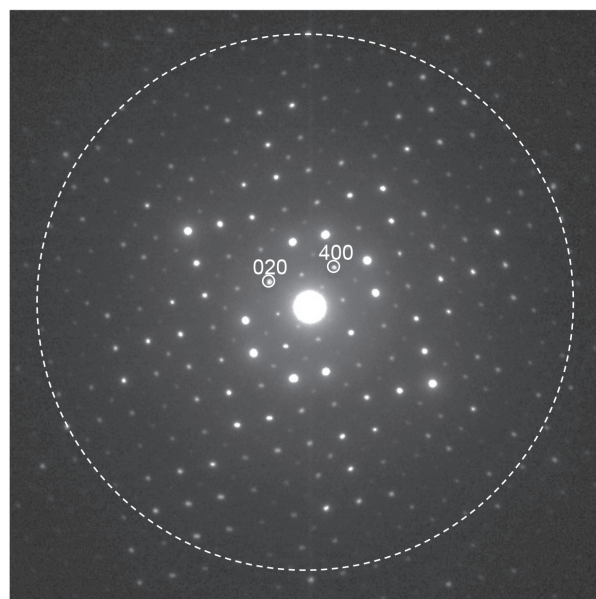
FIGURE 2. [001] zone-axis PED pattern (precession angle 2.8°) obtained on the heat-treated sample. The dashed circle corresponds to the resolution limit $g^{max} = 1.4$ Å^{-1} for data extraction.


FIGURE 1. TEM images of (**a**) the untreated sample and (**b**) the heat-treated sample. Circles indicate the analyzed areas (1, 2, and 3).

TABLE 3. Refinement results for PED data sets obtained on the heat-treated sample

Data set	$wR2$	t (nm)	X_{Fe}(M1)	X_{Fe}(M2)	Q^*	Mg/(Fe+Mg)
Precession angle: 1.6°						
opht1p1.6	12.88	52(2)	0.200(15)	0.420(15)	0.220(15)	0.69
opht2p1.6	13.18	46(2)	0.235(15)	0.415(15)	0.180(15)	0.68
opht3p1.6	20.58	49(2)	0.280(15)	0.420(15)	0.140(15)	0.65
Precession angle: 2.4°						
opht1p2.4	6.77	49(2)	0.147(10)	0.430(10)	0.283(15)	0.71
opht2p2.4	9.53	43(2)	0.134(10)	0.441(10)	0.307(15)	0.71
opht3p2.4	12.30	49(2)	0.140(10)	0.452(10)	0.312(15)	0.70
Precession angle: 2.8°						
opht1p2.8	7.38	49(2)	0.154(10)	0.442(10)	0.288(20)	0.70
opht2p2.8	8.66	43(2)	0.134(10)	0.458(10)	0.324(20)	0.70
opht3p2.8	11.04	46(2)	0.154(10)	0.458(10)	0.304(20)	0.69

Notes: Labels include the area location (1, 2, or 3) and the precession angle. All data sets were collected using selected area diffraction.
* $Q = X_{Fe}$(M2) – X_{Fe}(M1).
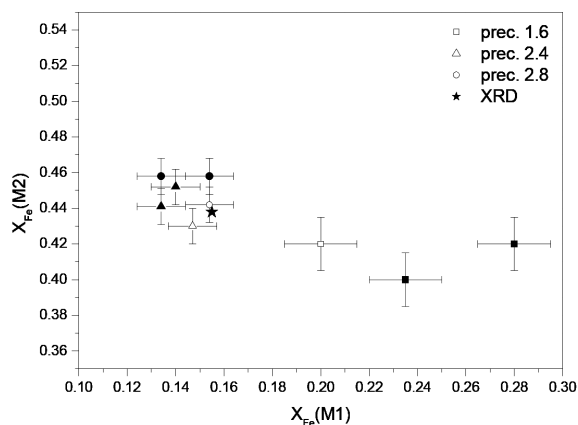
FIGURE 3. Plot of X_{Fe}(M2) vs. X_{Fe}(M1) for the heat-treated sample. Squares: precession angle 1.6°, triangles: 2.4° and circles: 2.8°. Empty symbols: area 1, gray symbol: area 2, full dark symbol: area 3 (see Fig. 1b). The black star corresponds to XRD data as obtained on the single crystal (error bars ca. size of the symbol).

(2013) leads to the same range of values for the uncertainties.

Results obtained with precession angle 1.6° are inconsistent with those obtained with 2.4° and 2.8°, leading to quite different X_{Fe}(M1) and X_{Fe}(M2) values (Fig. 3). A higher dispersion of the results is also observed with precession angle 1.6° together with larger estimated errors of the three parameters. The larger errors are associated with the shape of the $wR2$ surface at 1.6° precession angle, which is much flatter than those obtained at 2.4° and 2.8° (Fig. 4), making $wR2$ less sensitive to X_{Fe}(M1) and X_{Fe}(M2).

Results obtained with 2.4° and 2.8° data sets overlap within their standard deviation for X_{Fe}(M1) and X_{Fe}(M2) whatever the observed area and the precession angle. The resulting mean values and dispersions are X_{Fe}(M1) = 0.144 ± 0.008 and X_{Fe}(M2) = 0.447 ± 0.010. These values are consistent with those derived from XRD data [X_{Fe}(M1) = 0.155(2) and X_{Fe}(M2) = 0.438(2)]. The thicknesses as deduced from data sets with precession angles 2.4° and 2.8° are also consistent, giving $t = 49 ± 1.5$ nm for area 1, $t = 43 ± 1.5$ for area 2 and $t = 47.5 ± 1.5$ nm for area 3.

Untreated sample

On the untreated sample, analysis has been performed using precession angles 2.4° and 2.8° for three areas of the TEM specimen. Results are summarized in Table 4 and plotted on Figure 5. Note that for the first area, 5 data sets are available: 3 of them have been acquired using microdiffraction (oplt1Ap24, oplt1Ap28, and oplt1Bp28) and the remaining using selected area diffraction. For areas 2 and 3, all the data have been acquired using selected area diffraction.

Slight discrepancies are obtained at the three areas as a function of the precession angles. Discrepancies are also observed between microdiffraction and selected area data sets taken on area 1 with 2.4° precession angle [compare oplt1Ap2.4 (microdiffraction) and oplt1Bp2.4 (selected area)]. Results are more consistent using 2.8° precession angle [compare oplt1Ap2.8 and oplt1Bp2.8 (microdiffraction) with oplt1Cp2.8 (selected area)]. Overall, a larger dispersion of the results is observed compared to the heat-treated sample, leading to mean values and dispersions X_{Fe}(M1) = 0.069 ± 0.016 and X_{Fe}(M2) = 0.551 ± 0.028. Despite the small discrepancy between X_{Fe}(M1) obtained with PED and with XRD [X_{Fe}(M1) = 0.029(2) and X_{Fe}(M2) = 0.554(2)], the agreement is once again satisfactory.

DISCUSSION

It follows clearly from Figures 3 and 5 that the present method enables the distinction of the Opx samples as a function of their ordering state. This distinction is emphasized in Figure 6, where all the data have been plotted together (only the inconsistent data with precession angle 1.6° have been removed). Furthermore, values obtained for site occupancies are globally consistent with those obtained using XRD at the millimeter scale. To our knowledge, this is the first successful demonstration that site occupancies can be determined quantitatively at submicrometer scale using precession electron diffraction. Even if the dispersion of the results is still high compared to that obtained using XRD and has to be lowered for quantitative exploitation, this result opens the door to a wide range of applications in the field of the study of minerals at the submicrometer scale and their potential use as geothermometers and speedometers. In this section, we discuss the influence of experimental parameters on the accuracy of the results, namely the precession angle and the initial orientation of the sample. Possible structural heterogeneity in the untreated sample is then inferred.

Influence of the precession angle and of the sample orientation

Two points require detailed discussion. First, concerning the heat-treated sample (Table 3; Fig. 3), results obtained with precession angle 1.6° are inconsistent with those obtained with 2.4° and 2.8° and should be discarded. Second, results obtained on the various areas of the untreated sample with 2.4° and 2.8° precession angles do not strictly overlap within their uncertainties (Table 4; Fig. 5). These points suggest that the occupancy determination could depend on the precession angle. However, calculation of diffracted intensities for comparison with experimental data takes into account the value of the precession angle and results should therefore not depend on it. Nevertheless, as described in the section on data analysis, another important experimental parameter has not been taken into account in the simulations of the PED intensities, namely the accurate orientation of the sample with respect to the precession hollow cone axis.
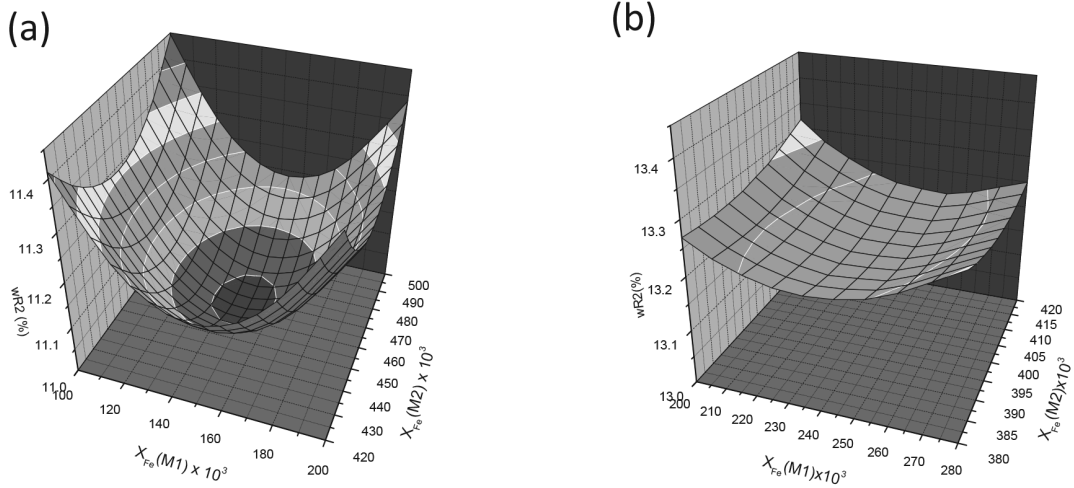
FIGURE 4. Plot of $wR2$ as a function of $X_{Fe}(M1)$ and $X_{Fe}(M2)$ for the heat-treated sample. (**a**) Precession angle 2.8°, area 3. (**b**) Precession angle 1.6°, area 2.

TABLE 4. Refinement results for PED data sets obtained on the untreated sample

Data set	$wR2$	t (nm)	$X_{Fe}(M1)$	$X_{Fe}(M2)$	Q^*	Mg/(Fe+Mg)
		Precession angle: 2.4°				
oplt1Ap2.4[1]	12.80	43(2)	0.030(10)	0.582(10)	0.552(15)	0.69
oplt1Bp2.4	9.42	40(2)	0.067(10)	0.544(10)	0.447(15)	0.69
oplt2p2.4	7.39	40(2)	0.092(10)	0.502(10)	0.410(15)	0.70
oplt3p2.4	17.89	40(2)	0.081(10)	0.572(10)	0.491(15)	0.67
		Precession angle: 2.8°				
oplt1Ap2.8[1]	9.60	43(2)	0.072(10)	0.544(10)	0.472(15)	0.69
oplt1Bp2.8[1]	9.35	40(2)	0.072(10)	0.535(10)	0.463(15)	0.70
oplt1Cp2.8	9.26	40(2)	0.067(10)	0.563(10)	0.496(15)	0.69
oplt2p2.8	15.11	40(2)	0.072(10)	0.595(10)	0.523(15)	0.67
oplt3p2.8	10.90	40(2)	0.072(10)	0.526(10)	0.454(15)	0.70

Notes: Labels include the area location (1, 2, or 3) and the precession angle. All data sets were collected using selected-area electron diffraction except oplt1Ap2.4, oplt1Ap2.8, and oplt1Bp2.8, which correspond to microdiffraction.
$^* Q = X_{Fe}(M2) - X_{Fe}(M1)$.
[1] Microdiffraction.

Let us call Θ the value of the angle between the steady incident beam direction and the crystal zone axis (Fig. 7). When $\Theta = 0$ (Fig. 7a), the on-axis orientation is perfect and for each diffraction vector, the excitation error S_g is equal to that of the opposite vector S_{-g}. When $\Theta \neq 0$ (Fig. 7b), $S_g \neq S_{-g}$ and consequently $I_g \neq I_{-g}$. It is one of the principal advantages of the precession method to suppress the influence of the sample misorientation by acquiring the integrated value of intensities I_g^{int} (Fig. 7c) instead of a particular value $I_g(S_g)$ as in the steady beam configuration. To fully exploit this advantage, the precession angle φ should be high with respect to Θ, otherwise integration of the intensities is not complete and still depends on the orientation of the sample. This is particularly true for the intense reflections close to the center of the diffraction pattern (small g vectors). It is thus likely that the dispersion of the results as a function of the precession angle occurs due to the imperfect alignment of the zone axis with respect to the non-precessed electron beam, which is indeed not exactly known and difficult to quantify for a given data set. This effect is most important for low-precession angles, since the integration of the intensities is then only partial. As a matter

of fact, results obtained with the same data sets but including beam orientation refinement (Palatinus et al. 2013) reveal a lower sensitivity of the refined occupancies to the precession angle, and thus support the present interpretation. Therefore, in a first approach, we suggest using high-precession angles (larger than 2°) for the data collection, and orienting the crystal very carefully. The residual effect of misalignment should then be very small. Repeating the experiment several times on the same area is a further means of improving the accuracy.

Untreated sample heterogeneity

For the untreated sample, there is a systematic discrepancy between the $X_{Fe}(M1)$ and $X_{Fe}(M2)$ values deduced from PED and XRD. Furthermore, independently of the inaccuracy of the
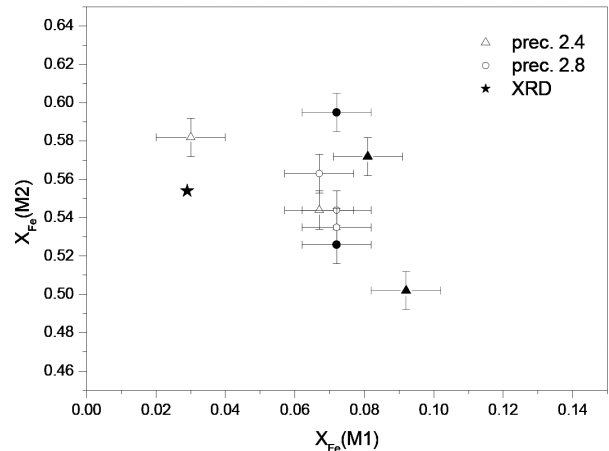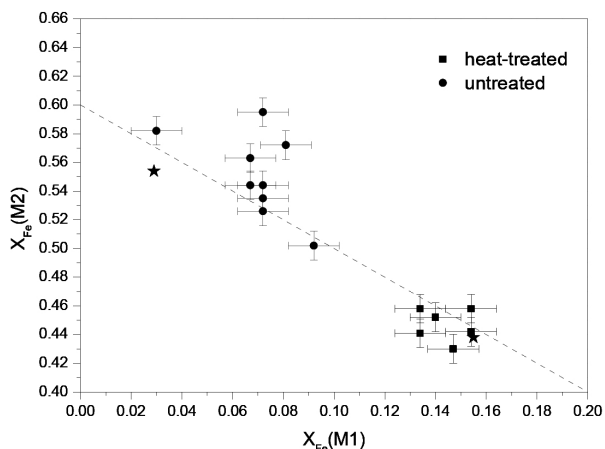

FIGURE 5. Plot of $X_{Fe}(M2)$ vs. $X_{Fe}(M1)$ for the untreated sample. Triangles: precession angle 2.4° and circles: precession angle 2.8°. Empty symbols: area 1, gray symbol: area 2, full dark symbol: area 3 (see Fig. 1a). The black star corresponds to XRD data as obtained as obtained on the single crystal (error bars ca. size of the symbol).

FIGURE 6. Plot of $X_{Fe}(M2)$ vs. $X_{Fe}(M1)$ for the untreated (gray circles) and heat-treated (black squares) samples. Black stars correspond to XRD data (error bars ca. size of the symbol). The dashed-line corresponds to the constant composition line with Mg/(Mg+Fe) = 0.70.

sample orientation, results on $X_{Fe}(M1)$ and $X_{Fe}(M2)$ are more dispersed for the untreated sample than for the heat-treated one (Fig. 6). All parameters for PED data acquisition and analysis being equivalent for both samples (except for the actual beam orientation, cf. the previous section), this strongly suggests an influence of the samples themselves. Indeed, the heat-treated (disordered) sample has been thermally homogenized at high temperature, whereas no treatment has been made on the natural sample (ordered). The untreated sample may thus present local composition or ordering heterogeneities. Such structural heterogeneities may explain both the larger dispersion of the PED results and the discrepancy between XRD and PED results obtained on this sample.

The heterogeneity of the untreated sample is highlighted when plotting the line of constant composition in the graph of $X_{Fe}(M2)$ as a function of $X_{Fe}(M1)$ (Fig. 6). This line is obtained using the relation $X_{Fe}(M2) = 2(1 - y) - X_{Fe}(M1)$, where y is the ratio Mg/(Fe+Mg). Obviously, the dispersion of the results around the line drawn for $y = 0.70$ (as given by the electron microprobe analysis at the grain scale) is much more pronounced for the untreated
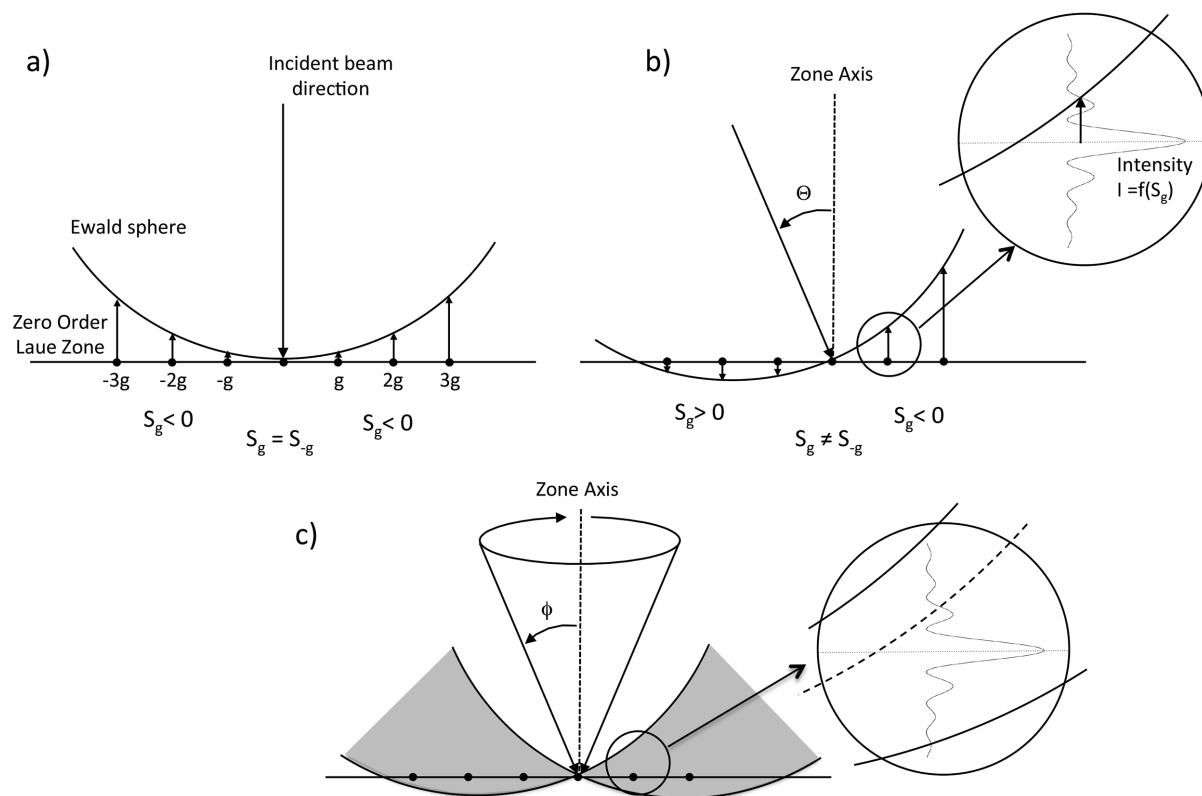
FIGURE 7. Sketch of the variation of the intensity of a **g** diffraction vector as a function of the orientation of the incident beam. S_g is the vector pointing from the reciprocal lattice node to the Ewald sphere. S_g is positive when oriented along the beam direction and negative elsewhere. (**a**) The incident beam is perfectly aligned along the zone axis and $S_g = S_{-g}$. (**b**) The incident beam is tilted with an angle φ from the zone-axis orientation. Then $S_g \neq S_{-g}$. (**c**) When the beam is rotated, the intensities are integrated along the S values. For the integration to be sufficiently complete, the precession angle has to be high enough.

sample than for the heat-treated one. At this point, two types of dispersion should be distinguished: dispersion along the line corresponds to the variation of site occupancies (order parameter) at constant composition, whereas results deviating from the line correspond to compositional variations. In the case of the untreated sample, both kinds of dispersion are present, suggesting order parameter variation as well as composition variation along the sample at a submicrometer scale. The maximum Mg/(Mg+Fe) variation deduced from our analysis is around 4% (see Table 4). While order parameter variation involving short-range diffusion processes is plausible at this scale, composition variation is more unlikely. EDX composition profile acquired across the studied areas revealed no composition fluctuation higher than the sensitivity of the EDX method, i.e., around 2% on the Mg/(Fe+Mg) ratio. This suggests that data sets resulting in a too high deviation (superior to 2%) from the constant composition line are probably influenced by the imperfection of the model, especially by neglecting the variation of the sample orientation. This is confirmed by results obtained using orientation refinement (Palatinus et al. 2013), which are mainly dispersed along the constant composition line, corresponding to ordering variations at a microscopic scale.

CONCLUDING REMARKS

To our knowledge, this work on the structural ordering in orthopyroxene is the first demonstration of a quantitative determination of site occupancies at submicrometer scale using precession electron diffraction. Even if quantitative exploitation of the results for deciphering thermal history of the sample is still doubtful due to the high dispersion of the results, precision is largely sufficient to distinguish between a natural metamorphic Opx ordered structure from a disordered one obtained after annealing at high temperature and rapid quenching. The method should be sensitive enough to characterize even possible intermediate states of ordering.

There are other minerals in which the cationic distribution on non-equivalent sites depends on the cooling rate and closure temperature. This is for instance the case of clinopyroxene, for which equilibrium and kinetics of the disordering process has been already well studied by single-crystal XRD for augitic compositions (Brizi et al. 2000, 2001) and for low-Ca pigeonitic compositions (Pasqual et al. 2000; Domeneghetti et al. 2005; Alvaro et al. 2011). Along with orthopyroxenes, the latter are thus considered as potential geospeedometers. However, microtextural features present in many pyroxenes must be taken into account when dealing with accurate determination of cation distributions by XRD. For instance, orthopyroxenes and clinopyroxenes commonly show exsolution phenomena; in some favorable cases these can be assessed properly and the presence of exsolution products can be corrected for (Domeneghetti et al. 1996). Unfortunately, this has not been possible for pigeonite crystals bearing augite exsolutions, which is by far the most common case for pigeonite samples. This situation prevents the use of ordering processes in pigeonite as geospeedometrer for calculating cooling rates in meteorites. The use of PED thus opens a large field of application of geospeedometry using pigeonites, and may shed light on many complicated cooling histories of terrestrial rocks or of planetary bodies.

REFERENCES CITED

Alvaro, M., Cámara, F., Domenghetti, M.C., Nestola, F., and Tazzoli, V. (2011) HT $P2_1/c$–$C2/c$ phase transition and kinetics of Fe^{2+}–Mg order–disorder of an Fe-poor pigeonite: implications for the cooling history of ureilites. Contributions to Mineralogy and Petrology, 162, 599–613.

Blessing, R.H. (1995) An empirical correction for absorption anisotropy. Acta Crystallographica, A, 51, 33–38.

Boulahya, K., Ruiz-Gonzalez, L., Parras, M., Gonzalez-Calbet, J.M., Nickolsky, M.S., and Nicolopoulos, S. (2007) Ab initio determination of heavy oxide perovskite related structures from precession electron diffraction data. Ultramicroscopy, 107, 445–452.

Boullay, P., Dorcet, V., Perez, O., Grygiel, C., Prellier, W., Mercey, B., and Hervieu, M. (2009) Structure determination of a brownmillerite $Ca_2Co_2O_5$ thin film by precession electron diffraction. Physical Review B, 79, 184108.

Brizi, E., Molin, G.M., and Zanazzi, P.F. (2000) Experimental study of intracrystalline Fe^{2+}–Mg exchange in three augite crystals: Effect of composition on geothermometric calibration. American Mineralogist, 85, 1375–1382.

Brizi, E., Molin, G.M., Zanazzi, P.F., and Merli, M. (2001) Ordering kinetics of Mg-Fe^{2+} exchange in a $Wo_{43}En_{46}Fs_{11}$ augite. American Mineralogist, 86, 271–278.

Cámara, F., Doukhan, J.-C., Domeneghetti, M.C., and Zema, M. (2000) A TEM study of Ca-rich orthopyroxenes with exsolution products. European Journal of Mineralogy, 12, 735–748.

Domeneghetti, M.C., Tazzoli, V., Boffa-Ballaran, T., and Molin, G.M. (1996) Orthopyroxene from Serra de Magé meteorite: A structure refinement procedure for a $Pbca$ phase coexisting with $C2/c$ exsolved phase. American Mineralogist, 81, 842–846.

Domeneghetti, M.C., Zema, M., and Tazzoli, V. (2005) Kinetics of Fe^{2+}-Mg order-disorder in $P2_1/c$ pigeonite. American Mineralogist, 90, 1816–1823.

Dudka, A.P., Avilov, A.S., and Nicolopoulos, S. (2007) Crystal structure refinement using Bloch-wave method for precession electron diffraction. Ultramicroscopy, 107, 474–482.

Eggeman, A.S., White, T.A., and Midgley, P.A. (2010) Is precession electron diffraction kinematical? Part II: A practical method to determine the optimum precession angle. Ultramicroscopy, 110, 771–777.

Ganguly, J. (1982) Mg-Fe order-disorder in ferromagnesian silicates. II. Thermodynamics, kinetics and geological applications. In S.K. Saxena, Ed., Advances in Physical Geochemistry, vol. 2, 58–99. Springer-Verlag, New York.

Ganguly, J., and Tazzoli, V. (1994) Fe^{2+}-Mg Interdiffusion in ortho-pyroxene—retrieval from the data on intracrystalline exchange-reaction. American Mineralogist, 79, 930–937.

Gemmi, M., and Nicolopoulos, S. (2007) Structure solution with three-dimensional sets of precessed electron diffraction intensities. Ultramicroscopy, 107, 483–494.

Gemmi, M., Klein, H., Rageau, A., Strobel, P., and Le Cras, F. (2010) Structure solution of the new titanate $Li_4Ti_8Ni_3O_{21}$ using precession electron diffraction. Acta Crystallographica, B66, 60–68.

Gjønnes, K., Cheng, Y.F., Berg, B.S. Hansen, V.A.F., Gjønnes, K., Cheng, Y.F., Berg, B.S., and Hansen, V. (1998) Corrections for multiple scattering in integrated electron diffraction intensities. Application to determination of structure factors in the [001] projection of Al_mFe. Acta Crystallographica, A54, 102–119.

Hadermann, J., Abakumov, A.M., Tsirlin, A.A., Filonenko, V.P., Gonnissen, J., Tan, H., Verbeeck, J., Gemmi, M., Antipov, E.V., and Rosner, H. (2010) Direct space structure solution from precession electron diffraction data: Resolving heavy and light scatterers in $Pb_{13}Mn_9O_{25}$. Ultramicroscopy, 110, 881–890.

Hadermann, J., Abakumov, A.M., Turner, S., Hafideddine, Z., Khasanova, N.R., Antipov, E.V., and Van Tendeloo, G. (2011) Solving the structure of Li ion battery materials with precession electron diffraction: Application to Li_2CoPO_4F. Chemistry of Materials, 23, 3540–3545.

Hawthorne, F.C., Ungaretti, L., and Oberti, R. (1995) Site populations in minerals: Terminology and presentation of results of crystal-structure refinement. Canadian Mineralogist, 33, 907–911.

Heinemann, R., Kroll, H., and Langenhorst, F. (2008) Relationship between Guinier-Preston zones and the kinetics of the intracrystalline Fe^{2+}, Mg exchange reaction in Johnstown meteoritic orthopyroxene. European Journal of Mineralogy, 20, 551–561.

Ibers, J.A., and Hamilton, W.C. (1974) International Tables for X-ray Crystallography. Kynoch Press, Birmingham, U.K., vol. 4., 99–101.

Klein, H. (2011) Precession electron diffraction of Mn_2O_3 and $PbMnO_{2.75}$: solving structures where X-rays fail. Acta Crystallographica, A67, 303–309.

Merli, M., Cámara, F., Domeneghetti, C., and Tazzoli, V. (2002) Leverage analysis

of X-ray single crystal diffraction data from orthopyroxene and pigeonite. European Journal of Mineralogy, 14, 773–784.

Mugnaioli, E., Gorelik, T., and Kolb, U. (2009) "Ab initio" structure solution from electron diffraction data obtained by a combination of automated diffraction tomography and precession technique. Ultramicroscopy, 109, 758–765.

Oleynikov, P., Hovmoller, S., and Zou, X.D. (2007) Precession electron diffraction: Observed and calculated intensities. Ultramicroscopy, 107, 523–533.

Own, C.S., Marks, L.D., and Sinkler, W. (2006) Precession electron diffraction 1: multislice simulation. Acta Crystallographica, A62, 434–443.

Palatinus, L. (2011) PETS—program for analysis of electron diffraction data. Institute of Physics of the AS CR, Prague, Czechia.

Palatinus, L., Klementova, M., Drinek, V., Jarosova, M., and Petricek, V. (2011) An incommensurately modulated structure of η'-Phase of $Cu_{3+x}Si$ determined by quantitative electron diffraction tomography. Inorganic Chemistry, 50, 3743–3751.

Palatinus, L., Jacob, D., Cuvillier, P., Klementova, M., Sinkler, W., and Marks, L.D. (2013) Structure refinement from precession electron diffraction data. Acta Crystallographica, A69, 171–188.

Pasqual, D., Molin, G., and Tribadino, M. (2000) Single-crystal thermometric calibration of Fe-Mg order-disorder in pigeonites. American Mineralogist, 85, 953–962.

Sheldrick, G.M. (1996) SADABS. Institüt für Anorganische Chemie der Universität. Göttingen, Germany.

——— (2008) A short history of SHELX. Acta Crystallographica, A64, 112–122.

Sinkler, W., and Marks, L.D. (2010) Characteristics of precession electron diffraction intensities from dynamical simulations. Zeitschrift für Kristallographie, 225, 47–55.

Song, K., Kim, Y.J., Kim, Y.I., and Kim, J.G. (2012) Application of theta-scan precession electron diffraction to structure analysis of hydroxyapatite nanopowder. Journal of Electron Microscopy, 61, 9–15.

Stadelmann, P. (2004) JEMS, Electron Microscopy Software, java version, CIME-EPFL, CH 1015 Lausanne 2004.

Stimpfl, M., Ganguly, J., and Molin, G. (1999) Fe^{2+}-Mg order-disorder in orthopyroxene: equilibrium fractionation between the octahedral sites and thermodynamic analysis. Contributions to Mineralogy and Petrology, 136, 297–309.

——— (2005) Kinetics of Fe^{2+}–Mg order–disorder in orthopyroxene: experimental studies and applications to cooling rates of rocks. Contributions to Mineralogy and Petrology, 150, 319–334.

Tarantino, S.C., Domeneghetti, M.C., Carpenter, M.A., Shaw, C.J.S., and Tazzoli, V. (2002) Mixing properties of the enstatite-ferrosilite solid solution: I. A macroscopic perspective. European Journal of Mineralogy, 14, 525–536.

Tribaudino, M., and Talarico, F. (1992) Orthopyroxenes from granulite rocks of the Wilson Terrane (Victoria Land, Antarctica); crystal chemistry and cooling history. European Journal of Mineralogy, 4, 453–463.

Vincent, R., and Midgley, P.A. (1994) Double conical beam-rocking system for measurement of integrated electron diffraction intensities. Ultramicroscopy, 53, 271–282.

White, T.A., Moreno, M.S., and Midgley, P.A. (2010) Structure determination of the intermediate tin oxide Sn_3O_4 by precession electron diffraction. Zeitschrift für Kristallographie, 225, 56–66.

Zema, M., Domeneghetti, M.C., and Tazzoli, V. (1999) Order-disorder kinetics in orthopyroxene with exsolution products. American Mineralogist, 84, 1895–1901.